Theoretical study of time-dependent, ultrasound-induced acoustic streaming in microchannels

Peter Barkholt Muller[*] and Henrik Bruus[†]

Department of Physics, Technical University of Denmark, DTU Physics Building 309, DK-2800 Kongens Lyngby, Denmark

Based on first- and second-order perturbation theory, we present a numerical study of the temporal buildup and decay of unsteady acoustic fields and acoustic streaming flows actuated by vibrating walls in the transverse cross-sectional plane of a long straight microchannel under adiabatic conditions and assuming temperature-independent material parameters. The unsteady streaming flow is obtained by averaging the time-dependent velocity field over one oscillation period, and as time increases, it is shown to converge towards the well-known steady time-averaged solution calculated in the frequency domain. Scaling analysis reveals that the acoustic resonance builds up much faster than the acoustic streaming, implying that the radiation force may dominate over the drag force from streaming even for small particles. However, our numerical time-dependent analysis indicates that pulsed actuation does not reduce streaming significantly due to its slow decay. Our analysis also shows that for an acoustic resonance with a quality factor Q, the amplitude of the oscillating second-order velocity component is Q times larger than the usual second-order steady time-averaged velocity component. Consequently, the well-known criterion $v_1 \ll c_s$ for the validity of the perturbation expansion is replaced by the more restrictive criterion $v_1 \ll c_s/Q$. Our numerical model is available as supplemental material in the form of COMSOL model files and MATLAB scripts.

I. INTRODUCTION

Acoustophoresis has successfully been used in many applications to manipulate particles in the size range from about 0.5 mm down to about 2 μm [1]. However, for smaller particles, the focusing by the acoustic radiation force is hindered by the drag force from the suspending liquid, which is set in motion by the generation of an acoustic streaming flow [2,3]. This limits the use of acoustophoresis to manipulate submicrometer particles, relevant for application within medical, environmental, and food sciences, and it underlines a need for better understanding of acoustic streaming and ways to circumvent this limitation.

The phenomenon of acoustic streaming was first described theoretically by Lord Rayleigh [4] in 1884, and has later been revisited, among others, by Schlicting [5], Nyborg [6], Hamilton [7,8], Rednikov and Sadhal [9], and Muller *et al.* [10], to extend the fundamental treatment of the governing equations and to solve the equations for various open and closed geometries.

Numerical methods have been applied in many studies to predict the streaming phenomena observed in various experiments. Muller *et al.* [2] developed a numerical scheme to solve the acoustic streaming in the cross section of a long straight microchannel, which resolved the viscous acoustic boundary layers and described the interplay between the acoustic scattering force and the streaming-induced drag force on suspended particles. This scheme was later extended to take into account the thermoviscous effects arising from the dependence of the fluid viscosity on the oscillating temperature field [11]. Lei *et al.* [12,13] have developed a numerical scheme based on the effective slip-velocity equations, originally proposed by Nyborg in 1953 [14,15], which avoid the resolution of the thin

boundary layers but still enable qualitative predictions of the three-dimensional streaming flows observed in microchannels and flat microfluidic chambers. To obtain quantitative results from such models that do not resolve the acoustic boundary layers, Hahn *et al.* [16] developed an effective model to determine the loss associated with the viscous stresses inside the thermoacoustic boundary layers, and apply this loss as an artificial bulk absorption coefficient. This enables the calculation of correct acoustic amplitudes, without resolving the thin acoustic boundary layers. Acoustic streaming in the cross section of a straight PDMS microchannel excited by surface acoustic waves was studied numerically by Nama *et al.* [17], describing the influence of the acoustically soft PDMS wall on the particle focusability, and examining the possibilities of having two tunable counterpropagating surface acoustic waves.

All of the above-mentioned studies consider steady acoustic streaming flows. This is reasonable as the streaming flow reaches steady state typically in a few milliseconds, much faster than other relevant experimental time scales. Furthermore, this allows for analytical solutions for the streaming velocity field in some special cases, and it makes it much easier to obtain numerical solutions. However, an experimental study by Hoyos and Castro [18] indicates that a pulsed actuation, instead of steady, can reduce the drag force from the streaming flow relative to the radiation force and thus allow the latter also to dominate manipulation of submicrometer particles. This might provide an alternative method to the one proposed by Antfolk *et al.* [19], which used an almost square channel with overlapping resonances to create a streaming flow that did not counteract the focusing of submicrometer particles.

To theoretically study the effects of a pulsed ultrasound actuation, we need to solve the temporal evolution of the acoustic resonance and streaming, which is the topic of the present work. Numerical solutions of the time-domain acoustic equations were used by Wang and Dual [20] to calculate the time-averaged radiation force on a cylinder and the steady streaming

around a cylinder, both in a steady oscillating acoustic field. However, they did not present an analysis of the unsteady buildup of the acoustic resonance and the streaming flow.

In this paper, we derive the second-order perturbation expansion of the time-dependent governing equations for the acoustic fields and streaming velocity, and solve them numerically for a long straight channel with acoustically hard walls and a rectangular cross section. The analysis and results are divided into two sections: (1) A study of the transient buildup of the acoustic resonance and streaming from a initially quiescent state towards a steady oscillating acoustic field and a steady streaming flow. (2) An analysis of the response of the acoustic field and the streaming flow to pulsed actuation, and quantifying whether this can lead to better focusability of submicrometer particles.

In previous studies, such as [2,11,17], only the periodic state of the acoustic resonance and the steady time-averaged streaming velocity are solved. When solving the time-dependent equations, we obtain a transient solution, which may also be averaged over one oscillation period to obtain an unsteady time-averaged solution.

II. BASIC ADIABATIC ACOUSTIC THEORY

In this section we derive the governing equations for the first- and second-order perturbations to unsteady acoustic fields in a compressible Newtonian fluid. We only consider acoustic perturbation in fluids, and treat the surrounding solid material as ideal rigid walls, a good approximation for water channels in glass-silicon systems. Moreover, extensive theoretical and experimental work [2,3,10,11,19,21] has shown that the adiabatic model describes the observed phenomena qualitatively correctly, while thermoviscous effects may lead to relative quantitative changes up to 30%. Thus by employing an adiabatic model, we can provide an analysis of experimental relevance while at the same time restricting the complexity and vast parameter space of the full problem. We leave a more complete thermoviscous analysis to future work. Our treatment is based on textbook adiabatic acoustics [22] and our previous study Ref. [11] of the purely periodic state.

A. Adiabatic thermodynamics

We employ the adiabatic approximation, which assumes that the entropy is conserved for any small fluid volume [23]. Consequently, the thermodynamic state of the fluid is described by only one independent thermodynamic variable, which we choose to be the pressure p. See Table I for parameter values. The changes $d\rho$ in the density ρ from the equilibrium state are given by

$$d\rho = \rho \kappa_s \, dp, \tag{1}$$

where the isentropic compressibility κ_s is defined as

$$\kappa_s = \frac{1}{\rho}\left(\frac{\partial \rho}{\partial p}\right)_s = \frac{1}{\rho c_s^2}. \tag{2}$$

B. Governing equations

Mass conservation implies that the rate of change $\partial_t \rho$ of the density in a test volume with surface normal vector $\boldsymbol{n}$ is

TABLE I. IAPWS parameter values for pure water at ambient temperature 25 °C and pressure 0.1013 MPa. For references see Sec. II B in Ref. [11].

Parameter	Symbol	Value	Unit
Acoustic properties:			
Mass density	ρ_0	9.971×10^2	kg m^{-3}
Speed of sound	c_s	1.497×10^3	m s^{-1}
Compressibility	κ_s	4.477×10^{-10}	Pa^{-1}
Transport properties:			
Shear viscosity	η	8.900×10^{-4}	Pa s
Bulk viscosity	η^{b}	2.485×10^{-3}	Pa s

given by the influx (direction $-\boldsymbol{n}$) of the mass current density $\rho \boldsymbol{v}$. In differential form by Gauss's theorem it is

$$\partial_t \rho = \nabla \cdot [-\rho \boldsymbol{v}]. \tag{3a}$$

Substituting $\partial_t \rho$ and $\nabla \rho$ using Eq. (1), and dividing by ρ, the continuity equation (3a) becomes

$$\kappa_s \partial_t p = -\nabla \cdot \boldsymbol{v} - \kappa_s \boldsymbol{v} \cdot \nabla p. \tag{3b}$$

Similarly, momentum conservation implies that the rate of change $\partial_t(\rho \boldsymbol{v})$ of the momentum density in the same test volume is given by the stress forces $\boldsymbol{\sigma}$ acting on the surface (with normal $\boldsymbol{n}$), and the influx (direction $-\boldsymbol{n}$) of the momentum current density $\rho \boldsymbol{v} \boldsymbol{v}$. In differential form, neglecting body forces, this becomes

$$\partial_t(\rho \boldsymbol{v}) = \nabla \cdot [\boldsymbol{\tau} - p \, \boldsymbol{1} - \rho \boldsymbol{v} \boldsymbol{v}], \tag{4a}$$

where the viscous stress tensor is defined as

$$\boldsymbol{\tau} = \eta[\nabla \boldsymbol{v} + (\nabla \boldsymbol{v})^{\mathrm{T}}] + \left[\eta^{\mathrm{b}} - \tfrac{2}{3}\eta\right](\nabla \cdot \boldsymbol{v}) \, \boldsymbol{1}. \tag{4b}$$

Here $\boldsymbol{1}$ is the unit tensor and the superscript "T" indicates tensor transposition. Using the continuity equation (3a), the momentum equation (4a) is rewritten into the well-known Navier-Stokes form,

$$\rho \partial_t \boldsymbol{v} = \nabla \cdot [\boldsymbol{\tau} - p \, \boldsymbol{1}] - \rho(\boldsymbol{v} \cdot \nabla)\boldsymbol{v}, \tag{4c}$$

which is useful when solving problems in the time domain. Equations (3b) and (4c) constitute the nonlinear governing equations which we will study by applying the usual perturbation approach of small acoustic amplitudes.

C. First-order time-domain equations

The homogeneous, isotropic, quiescent thermodynamic equilibrium state is taken to be the zeroth-order state in the acoustic perturbation expansion. Following standard perturbation theory, all fields g are written in the form $g = g_0 + g_1$, for which g_0 is the value of the zeroth-order state, and g_1 is the acoustic perturbation which by definition has to be much smaller than g_0. For the velocity, the value of the zeroth-order state is $\boldsymbol{v}_0 = \boldsymbol{0}$, and thus $\boldsymbol{v} = \boldsymbol{v}_1$. The zeroth-order terms solve the governing equations in the zeroth-order state and thus drop out of the equations. Keeping only first-order terms, we obtain the following first-order equations.

The first-order continuity equation (3b) becomes

$$\kappa_s \partial_t p_1 = -\nabla \cdot \boldsymbol{v}_1, \tag{5}$$

and likewise, the momentum equation (4c) becomes

$$\rho_0 \partial_t \boldsymbol{v}_1 = \nabla \cdot [\boldsymbol{\tau}_1 - p_1 \mathbf{1}], \tag{6a}$$

where $\boldsymbol{\tau}_1$ is given by

$$\boldsymbol{\tau}_1 = \eta_0 [\nabla \boldsymbol{v}_1 + (\nabla \boldsymbol{v}_1)^{\mathrm{T}}] + \left[\eta_0^{\mathrm{b}} - \tfrac{2}{3}\eta_0\right](\nabla \cdot \boldsymbol{v}_1)\, \mathbf{1}. \tag{6b}$$

Equations (5) and (6) determine together with a set of boundary conditions the time evolution of the first-order acoustic fields p_1 and $\boldsymbol{v}_1$.

D. Second-order time-domain equations

Moving on to second-order perturbation theory, we write the fields as $g = g_0 + g_1 + g_2$, with g_1 and g_2 depending on both time and space. For simplicity and in contrast to Ref. [11], we do not include perturbations in η and η^{b}. This will cause the magnitude of the streaming to be slightly off, as does the adiabatic approximation; however the qualitative behavior is not expected to change. The second-order time-domain continuity equation (3b) becomes

$$\kappa_s \partial_t p_2 = -\nabla \cdot \boldsymbol{v}_2 - \kappa_s \boldsymbol{v}_1 \cdot \nabla p_1, \tag{7}$$

and the momentum equation (4c) takes the form

$$\rho_0 \partial_t \boldsymbol{v}_2 = -\rho_1 \partial_t \boldsymbol{v}_1 + \nabla \cdot [\boldsymbol{\tau}_2 - p_2\,\mathbf{1}] - \rho_0 (\boldsymbol{v}_1 \cdot \nabla)\boldsymbol{v}_1, \tag{8a}$$

where $\boldsymbol{\tau}_2$ is given by

$$\boldsymbol{\tau}_2 = \eta_0 [\nabla \boldsymbol{v}_2 + (\nabla \boldsymbol{v}_2)^{\mathrm{T}}] + \left[\eta_0^{\mathrm{b}} - \tfrac{2}{3}\eta_0\right](\nabla \cdot \boldsymbol{v}_2)\, \mathbf{1}. \tag{8b}$$

Using Eq. (1) in the form $\rho_1 = \rho_0 \kappa_s p_1$ and the first-order momentum equation (6a), we rewrite Eq. (8a) to

$$\begin{aligned}
\rho_0 \partial_t \boldsymbol{v}_2 =\ & \nabla \cdot \left[\boldsymbol{\tau}_2 - p_2\,\mathbf{1} - \kappa_s p_1 \boldsymbol{\tau}_1 + \tfrac{1}{2}\kappa_s p_1^2\,\mathbf{1}\right] \\
& + \kappa_s \nabla p_1 \cdot \boldsymbol{\tau}_1 - \rho_0 (\boldsymbol{v}_1 \cdot \nabla)\boldsymbol{v}_1.
\end{aligned} \tag{8c}$$

This particular form of the second-order momentum equation is chosen to minimize numerical errors as described in Sec. III A.

E. Periodic frequency-domain equations

When solving for the periodic state at $t \to \infty$, it is advantageous to formulate the first-order equations in the frequency domain. The harmonic first-order fields are all written as $g_1(\boldsymbol{r},t) = \mathrm{Re}\{g_1^{\mathrm{fd}}(\boldsymbol{r})e^{-i\omega t}\}$, where g_1^{fd} is the complex field amplitude in the frequency domain. The first-order frequency-domain equations are derived from Eqs. (5) and (6a) by the substitution $\partial_t \to -i\omega$,

$$\nabla \cdot \boldsymbol{v}_1^{\mathrm{fd}} - i\omega \kappa_s p_1^{\mathrm{fd}} = 0, \tag{9}$$

$$\nabla \cdot \left[\boldsymbol{\tau}_1^{\mathrm{fd}} - p_1^{\mathrm{fd}}\mathbf{1}\right] + i\omega \rho_0 \boldsymbol{v}_1^{\mathrm{fd}} = \mathbf{0}. \tag{10}$$

The steady time-averaged streaming flow is obtained from the time-averaged second-order frequency-domain equations, where $\langle g_2^{\mathrm{fd}}\rangle$ denotes time averaging over one oscillation period of the periodic second-order field. The time average of products of two harmonic first-order fields g_1^{fd} and $\tilde{g}_1^{\mathrm{fd}}$ is given by $\langle g_1^{\mathrm{fd}} \tilde{g}_1^{\mathrm{fd}}\rangle = \tfrac{1}{2}\,\mathrm{Re}\,[(g_1^{\mathrm{fd}})^* \tilde{g}_1^{\mathrm{fd}}]$, as in Ref. [11], where the asterisk denotes complex conjugation. In the periodic state, the fields may consist of harmonic terms and a steady term,

and thus all full time derivatives average to zero $\langle \partial_t g_2^{\mathrm{fd}}\rangle = 0$. The time-averaged second-order frequency-domain equations are derived from Eqs. (7) and (4a),

$$\nabla \cdot \langle \boldsymbol{v}_2^{\mathrm{fd}}\rangle + \kappa_s \langle \boldsymbol{v}_1^{\mathrm{fd}} \cdot \nabla p_1^{\mathrm{fd}}\rangle = 0, \tag{11}$$

$$\nabla \cdot \left[\langle \boldsymbol{\tau}_2^{\mathrm{fd}}\rangle - \langle p_2^{\mathrm{fd}}\rangle \mathbf{1} - \rho_0 \langle \boldsymbol{v}_1^{\mathrm{fd}} \boldsymbol{v}_1^{\mathrm{fd}}\rangle\right] = \mathbf{0}. \tag{12}$$

F. Acoustic energy and cavity Q factor

The total acoustic energy of the system in the time domain $E_{\mathrm{ac}}(t)$ and in the frequency domain $\langle E_{\mathrm{ac}}^{\mathrm{fd}}(\infty)\rangle$ is given by

$$E_{\mathrm{ac}}(t) = \int_V \left[\frac{1}{2}\kappa_s p_1^2 + \frac{1}{2}\rho_0 v_1^2\right] dV, \tag{13a}$$

$$\langle E_{\mathrm{ac}}^{\mathrm{fd}}(\infty)\rangle = \int_V \left[\frac{1}{2}\kappa_s \langle p_1^{\mathrm{fd}} p_1^{\mathrm{fd}}\rangle + \frac{1}{2}\rho_0 \langle \boldsymbol{v}_1^{\mathrm{fd}} \cdot \boldsymbol{v}_1^{\mathrm{fd}}\rangle\right] dV. \tag{13b}$$

Moreover, the time derivative of $E_{\mathrm{ac}}(t)$ is

$$\begin{aligned}
\partial_t E_{\mathrm{ac}} &= \int_V \partial_t \left[\frac{1}{2}\kappa_s p_1^2 + \frac{1}{2}\rho_0 v_1^2\right] dV \\
&= \int_V [\kappa_s p_1 \partial_t p_1 + \rho_0 \boldsymbol{v}_1 \cdot \partial_t \boldsymbol{v}_1]\, dV \\
&= \int_V \{\nabla \cdot [\boldsymbol{v}_1 \cdot (\boldsymbol{\tau}_1 - p_1\mathbf{1})] - \nabla \boldsymbol{v}_1 : \boldsymbol{\tau}_1\}\, dV,
\end{aligned} \tag{14a}$$

where we have used Eqs. (5) and (6a). Applying Gauss's theorem on the first term in Eq. (14a), we arrive at

$$\begin{aligned}
\partial_t E_{\mathrm{ac}} &= \int_A [\boldsymbol{v}_1 \cdot (\boldsymbol{\tau}_1 - p_1\mathbf{1})] \cdot \boldsymbol{n}\, dA - \int_V \nabla \boldsymbol{v}_1 : \boldsymbol{\tau}_1\, dV \\
&= P_{\mathrm{pump}} - P_{\mathrm{dis}},
\end{aligned} \tag{14b}$$

where P_{pump} is the total power delivered by the forced vibration of the sidewalls, and P_{dis} is the total power dissipated due to viscous stress. The quality factor Q of a resonant cavity is given by

$$Q = 2\pi \frac{\text{Energy stored}}{\text{Energy dissipated per cycle}} = \omega \frac{\langle E_{\mathrm{ac}}^{\mathrm{fd}}\rangle}{\langle P_{\mathrm{dis}}^{\mathrm{fd}}\rangle}. \tag{15}$$

G. Summary of theory

Throughout this paper we refer to two kinds of solutions of the acoustic energy and velocity fields: unsteady nonperiodic solutions obtained from Eqs. (5)–(8) and steady periodic solutions obtained from Eqs. (9)–(12). When presenting the unsteady nonperiodic solutions, they are often normalized by the steady periodic solution, to emphasize how close it has converged towards this solution.

III. NUMERICAL MODEL

As summarized in Sec. I, the vast majority of experimental work in the field of acoustophoresis deals with frequencies around $f \approx 10$ MHz, acoustic pressures of the order $p_1 = 0.1$ MPa, boundary layer widths $\delta < 500$ nm, and channel cross sections of dimensions near $h \approx 0.2$ mm. The key dimensional numbers are then low Mach numbers $\mathrm{MA} = v_1/c_0 = p_1/(\rho_0 c_0^2) \ll 10^{-3}$, fairly low acoustic Reynolds numbers
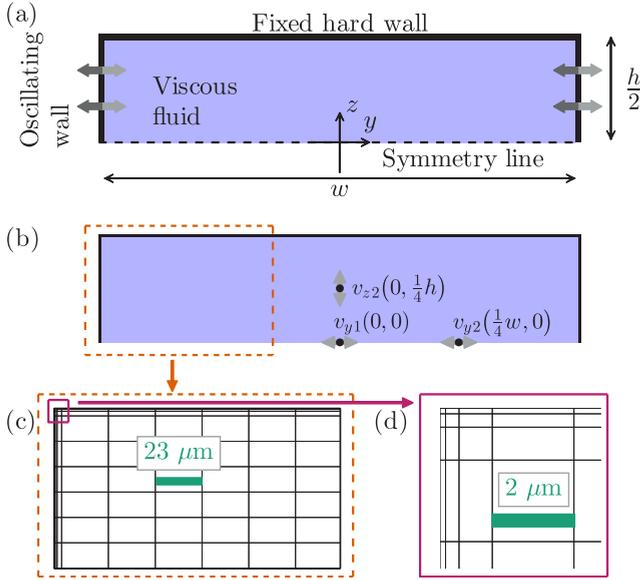
FIG. 1. (Color online) (a) Sketch of the rectangular computational domain in the yz plane representing the upper half of a rectangular cross section of a long straight microchannel of width $w = 380$ μm and height $h = 160$ μm as in Ref. [21]. The thick arrows indicate in-phase oscillating velocity actuation at the left and right boundaries. (b) The three black points indicate positions at which the velocity components (gray arrows), defined in Eq. (29) later in the paper, are probed. (c) Sketch of the spatial mesh used for the discretization of the physical fields. (d) A zoom-in on the mesh in the upper left corner.

Re $= v_1 h/\nu \lesssim 10$, and a small relative boundary-layer width $\delta/h \ll 0.01$. In accordance with this, we choose to model a specific system with parameters in this range: water at room temperature inside a rectangular microchannel embedded in a silicon-glass chip actuated at frequencies around 2 MHz; see Fig. 1. This system even has the added benefit of having been studied extensively and characterized well both theoretically and experimentally in the steady oscillatory state [2,3,10,11,19,21], thus providing a strong benchmark for the present analysis in the transient regime.

In more detail, the numerical scheme solves the governing equations for the acoustic field inside a water domain enclosed by a two-dimensional rectangular microchannel cross section. The vibrations in the surrounding silicon-glass chip and piezo transducer are not modeled. The water domain is surrounded by immovable hard walls, and the acoustic field is excited by oscillating velocity boundary conditions, representing an oscillating nm-sized displacement of the walls. A sketch of the numerical model is shown in Fig. 1(a). We exploit the symmetry along the horizontal center axis $z = 0$, reducing our computational domain by a factor of two. The system is also symmetric about the vertical center axis $y = 0$; however, our attempts to use this symmetry introduced numerical errors, and consequently it was not exploited in the numerical model. The model used to calculate the steady streaming flow in the time-periodic case is a simplification of the model presented in Ref. [11], whereas the model used to solve the time-dependent problem is new.

A. Governing equations

The governing equations are solved using the commercial software COMSOL MULTIPHYSICS [24] based on the finite element method [25]. To achieve greater flexibility and control, the equations are implemented through mathematics-weak-form-PDE modules and not through the built-in modules for acoustics and fluid mechanics. The governing equations are formulated to avoid evaluation of second-order spatial derivatives and of time derivatives of first-order fields in the second-order equations, as time derivatives carry larger numerical errors compared to the spatial derivatives. To fix the numerical solution of the second-order equations, a zero spatial average of the second-order pressure is enforced by a Lagrange multiplier. For the time-domain simulations we use the so-called generalized alpha solver [26–28]. This particular solver enables manual control of the numerical damping through the alpha parameter, and thus it is often applied in problems sensitive to numerical damping, such as in modeling of acoustics. In our numerical implementation, we have set the alpha parameter to 0.5 and used a fixed time step Δt. Furthermore, to limit the amount of data stored in COMSOL, the simulations are run from MATLAB [29] and long time-marching schemes are solved in shorter sections by COMSOL. COMSOL model files and MATLAB scripts are provided in the Supplemental Material [30].

B. Boundary conditions

The acoustic cavity is modeled with stationary hard rigid walls, and the acoustic fields are excited on the side walls by an oscillating velocity boundary condition with oscillation period t_0 and angular frequency ω,

$$t_0 = \frac{2\pi}{\omega}. \tag{16}$$

The symmetry of the bottom boundary is described by zero orthogonal velocity component and zero orthogonal gradient of the parallel velocity component. The explicit boundary conditions for the first-order velocity become

$$\text{top:} \quad v_{y1} = 0, \quad v_{z1} = 0, \tag{17a}$$

$$\text{bottom:} \quad \partial_z v_{y1} = 0, \quad v_{z1} = 0, \tag{17b}$$

$$\text{left-right:} \quad v_{y1} = v_{\text{bc}} \sin(\omega t), \quad v_{z1} = 0. \tag{17c}$$

The boundary conditions on the second-order velocity are set by the zero-mass-flux condition $\bm{n} \cdot \rho \bm{v} = 0$ on all boundaries, as well as zero parallel velocity component on the top, right, and left wall boundaries, and zero orthogonal derivative of the parallel component of the mass flux on the bottom symmetry boundary. The explicit boundary conditions for the second-order velocity become

$$\text{top:} \quad v_{y2} = 0, \quad v_{z2} = 0, \tag{18a}$$

$$\text{bottom:} \quad \partial_z \left(\rho_0 v_{y2} + \rho_1 v_{y1} \right) = 0, \quad v_{z2} = 0, \tag{18b}$$

$$\text{left-right:} \quad \rho_0 v_{y2} + \rho_1 v_{y1} = 0, \quad v_{z2} = 0. \tag{18c}$$

C. Spatial resolution

The physical fields are discretized using fourth-order basis functions for $\boldsymbol{v}_1$ and $\boldsymbol{v}_2$ and third-order basis functions for p_1 and p_2. The domain shown in Fig. 1(a) is covered by basis functions localized in each element of the spatial mesh shown in Fig. 1(c). Since the streaming flow is solved in the time domain, the computational time quickly becomes very long compared to the computational time of solving the usual steady streaming flow. Thus we have optimized the use of precious few mesh elements to obtain the best accuracy of the solution. We use an inhomogeneous mesh of rectangular elements ranging in size from 0.16 μm at the boundaries to 24 μm in the bulk of the domain. The convergence of the solution g with respect to a reference solution g_{ref} was considered through the relative convergence parameter $C(g)$ defined in Ref. [11] by

$$C(g) = \sqrt{\frac{\int (g - g_{\mathrm{ref}})^2 dy\,dz}{\int (g_{\mathrm{ref}})^2 dy\,dz}}. \tag{19}$$

In Ref. [11], $C(g)$ was required to be below 0.001 for the solution to have converged. The solution for the steady time-averaged velocity $\langle \boldsymbol{v}_2^{\mathrm{fd}}(\infty)\rangle$, calculated with the mesh shown in Figs. 1(c) and 1(d), has $C = 0.006$ with respect to the solution calculated with the fine triangular reference mesh in Ref. [11], which is acceptable for the present study.

D. Temporal resolution

The required temporal resolution for time-marching schemes is normally determined by the Courant-Friedrichs-Lewy (CFL) condition [31], also referred to as just the Courant number,

$$\mathrm{CFL} = \frac{c_s\,\Delta t}{\Delta r} \leqslant \mathrm{CFL}_{\mathrm{max}}, \tag{20}$$

where Δt is the temporal discretization and Δr is the spatial discretization. This means that the length over which a disturbance travels within a time step Δt should be some fraction of the mesh element size, ultimately ensuring that disturbances do not travel through a mesh element in one time step. A more accurate interpretation of the CFL condition is that it ensures that the error on the approximation of the time derivative is smaller than the error on the approximation of the spatial derivatives. Consequently, the value of $\mathrm{CFL}_{\mathrm{max}}$ depends on the specific solver and on the order of the basis functions. For fourth-order basis functions and the generalized alpha solver, Ref. [31] reports a value of $\mathrm{CFL}_{\mathrm{max}}^{\mathrm{4th}} = 0.05$, which is an empirical result for a specific model. Due to the inhomogeneity of the mesh, two values for the upper limit for the temporal resolution can be calculated based on Eq. (20): $\Delta t = 8 \times 10^{-10}$ s $\approx t_0/600$ for the bulk mesh size of 24 μm and $\Delta t = 5 \times 10^{-12}$ s $\approx t_0/95\,000$ for the boundary mesh size of 160 nm.

To determine a reasonable trade-off between numerical accuracy and computational time, we study the convergence of the transient solution towards the steady solution for different values of the temporal resolution $t_0/\Delta t$. The acoustic energy $E_{\mathrm{ac}}(t)$ is shown in Fig. 2(a) for different values of Δt and normalized by the steady time-averaged energy
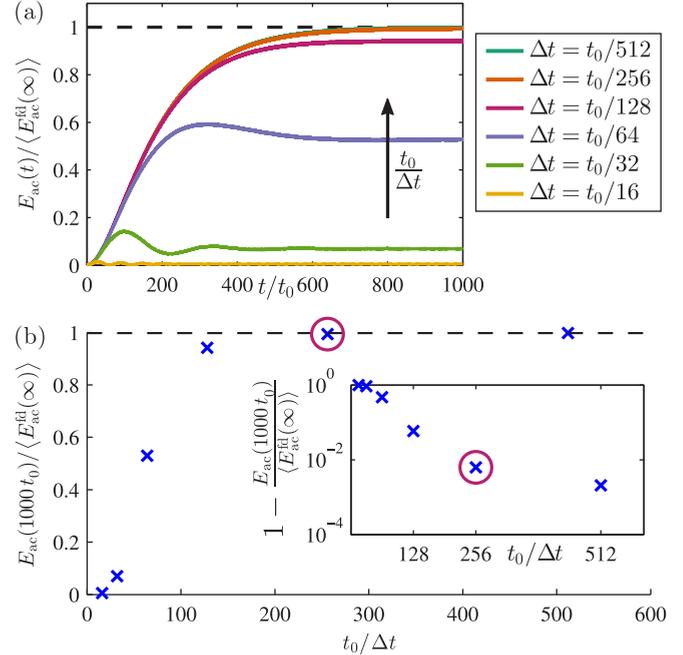

FIG. 2. (Color online) Numerical convergence and temporal resolution. (a) Graphs of the buildup of acoustic energy $E_{\mathrm{ac}}(t)$ in the time-domain simulations calculated with different fixed time steps Δt. The energy of the time-domain simulations is normalized with respect to the energy $\langle E_{\mathrm{ac}}^{\mathrm{fd}}(\infty)\rangle$ of the steady solution in the frequency domain, and should thus converge towards unity. In all simulations the actuation frequency equals the resonance frequency discussed in Sec. IV A. (b) Acoustic energy $E_{\mathrm{ac}}(1000\,t_0)$ at $t = 1000\,t_0$, normalized by $\langle E_{\mathrm{ac}}^{\mathrm{fd}}(\infty)\rangle$, and plotted versus the temporal resolution $t_0/\Delta t$ of the oscillation. The inset is a semilog plot of the relative deviation of $E_{\mathrm{ac}}(1000\,t_0)$ from $\langle E_{\mathrm{ac}}^{\mathrm{fd}}(\infty)\rangle$. The circled point in each graph indicates the time step $\Delta t = t_0/256$ used in all subsequent simulations.

$\langle E_{\mathrm{ac}}^{\mathrm{fd}}(\infty)\rangle$ of the frequency-domain calculation, and it is thus expected to converge to unity for long times. In Fig. 2(b), $E_{\mathrm{ac}}(1000t_0)/\langle E_{\mathrm{ac}}^{\mathrm{fd}}(\infty)\rangle$ is plotted versus the temporal resolution $t_0/\Delta t$, which shows how the accuracy of the time-domain solution increases as the temporal resolution is increased. In all subsequent simulations we have chosen a time step of $\Delta t = t_0/256$, the circled point in Fig. 2(b), for which the time-domain energy converges to 99.4% of the energy of the steady calculation. The chosen value for the time step is larger than the upper estimate $t_0/600$ of the necessary Δt based on the CFL condition. This might be because our spatial domain is smaller than the wavelength, and consequently a finer spatial resolution is needed, compared to what is usually expected to spatially resolve a wave.

We have noted that the fastest convergence is obtained when actuating the system at its (numerically determined) resonance frequency f_{res}. When shifting the actuation frequency half the resonance width $\frac{1}{2}\Delta f$ away from f_{res}, the energy $E_{\mathrm{ac}}(t)$ for $\Delta t = t_0/256$ converged to only 95% of the steady value $\langle E_{\mathrm{ac}}^{\mathrm{fd}}(\infty)\rangle$ (calculated in the frequency domain), thus necessitating smaller time steps to obtain reasonable convergence.

The computations where performed on a desktop PC with Intel Xeon CPU X5690 3.47 GHz 2 processors, 64-bit

Windows 7, and 128 GB RAM. The computations took approximately one hour for each time interval of width $100t_0$ with $\Delta t = t_0/256$, and the computational time was not limited by RAM, as only less than 2 GB RAM was allocated by COMSOL for the calculations.

IV. ONSET OF ACOUSTIC STREAMING

In this section the fluid is initially quiescent. Then, at time $t = 0$, the oscillatory velocity actuation is turned on, such that within the first oscillation period its amplitude increases smoothly from zero to its maximum value v_{bc}, which it maintains for the rest of the simulation. We study the resulting buildup of the acoustic resonance and the acoustic streaming flow.

A. Resonance and buildup of acoustic energy

To determine the resonance frequency, the steady acoustic energy $\langle E_{ac}^{fd}(\infty) \rangle$ Eq. (13b) was calculated for a range of frequencies based on the frequency-domain equations (9) and (10). In Fig. 3 the numerical results (circles) are shown together with a Gaussian fit (full line), while the inset exhibits the fitted resonance frequency f_{res}, the full width Δf at half maximum, and the quality factor $Q = f_{res}/\Delta f$.

The buildup of the acoustic energy in the cavity is well captured by a simple analytical model of a single sinusoidally driven damped harmonic oscillator with time-dependent position $x(t)$,

$$\frac{d^2x}{dt^2} + 2\Gamma\omega_0\frac{dx}{dt} + \omega_0^2 x = \frac{1}{m}F_0\sin(\omega t). \qquad (21)$$
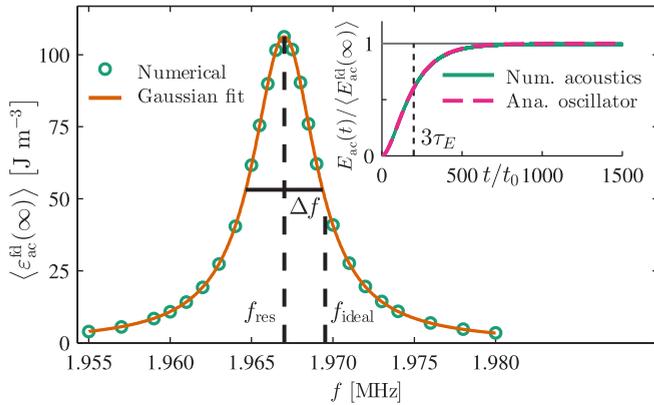
FIG. 3. (Color online) Resonance curve and buildup of acoustic energy. The numerical acoustic energy density $\langle E_{ac}^{fd}(\infty) \rangle/V$ (circles) for different frequencies of the boundary actuation and a Gaussian fit (full line) to the numerical data. $f_{res} = 1.9670094(7)$ MHz and $\Delta f = 4.727(2)$ kHz are the fitted resonance frequency at the center of the peak and the line width, while $f_{ideal} = c_s/(2w)$ is the frequency corresponding to matching a half wavelength with the channel width. The inset shows the numerical buildup of the acoustic energy (full line) for actuation at the resonance frequency, $\omega = 2\pi f_{res}$, along with the analytical prediction Eq. (23) (dashed line) for a single harmonic oscillator with the same resonance frequency and quality factor $Q = f_{res}/\Delta f = 416$. The resonance relaxation time is $\tau_E = Q/\omega = 66\,t_0$.

Here, Γ is the nondimensional loss factor, ω_0 is the resonance frequency of the oscillator, $\frac{1}{m}F_0$ is the amplitude of the driving force divided by the oscillator mass, and ω is the frequency of the forcing. The loss factor is related to the quality factor by $\Gamma = 1/(2Q)$, and in the underdamped case $\Gamma < 1$, the solution becomes

$$x(t) = A\left[\sin(\omega t + \phi) - \frac{\omega\, e^{-\Gamma\omega_0 t}}{\omega_0\sqrt{1-\Gamma^2}}\sin(\sqrt{1-\Gamma^2}\,\omega_0 t + \phi)\right]. \qquad (22)$$

The amplitude A and the phase shift ϕ between the forcing and the response are known functions of $\frac{F_0}{m}$, ω_0, ω, and Γ, which are not relevant for the present study. From Eq. (22) we obtain the velocity dx/dt, leading to the total energy E of the oscillator,

$$E = \frac{1}{2}m\omega_0^2 x^2 + \frac{1}{2}m\left(\frac{dx}{dt}\right)^2. \qquad (23)$$

Based on Eqs. (22) and (23), the characteristic time scale τ_E for the buildup of the acoustic energy is found to be

$$\tau_E = \frac{1}{2\Gamma\omega_0} = \frac{Q}{\omega_0}. \qquad (24)$$

The buildup of the energy in the single harmonic oscillator, calculated at $\omega = \omega_0$ with $\Gamma = 1.20 \times 10^{-3}$, is shown in the inset of Fig. 3 together with the buildup of acoustic energy $E_{ac}(t)$ of the microfluidic channel solved numerically at resonance, $\omega = 2\pi f_{res}$. The analytical and numerical results are in good agreement, and we conclude that the buildup of acoustic energy in the channel cavity can be modeled as a single harmonic oscillator. The energy builds up to 95% of its steady value in about $500\,t_0 \approx 8\,\tau_E$.

B. Decomposition of the velocity field

The task of calculating the buildup of the acoustic streaming flow is a multiscale problem, because the amplitude of the oscillating acoustic velocity field is several orders of magnitude larger than the magnitude of the streaming flow. This is indeed the very reason that we can apply the perturbation expansion

$$\boldsymbol{v} = \boldsymbol{v}_1 + \boldsymbol{v}_2, \qquad (25)$$

and decompose the nonlinear governing equations into a set of linear first-order equations and a set of second-order equations. However, there is also another level of difference in velocity scaling. In the purely periodic state, the velocity can be Fourier decomposed as

$$\boldsymbol{v}(\boldsymbol{r},t) = \boldsymbol{v}_1^\omega(\boldsymbol{r})\sin(\omega t) + \boldsymbol{v}_2^{2\omega}(\boldsymbol{r})\sin(2\omega t) + \boldsymbol{v}_2^0(\boldsymbol{r}), \qquad (26)$$

where $\boldsymbol{v}_1^\omega(\boldsymbol{r})$ is the steady amplitude of the first-order harmonic component, $\boldsymbol{v}_2^{2\omega}(\boldsymbol{r})$ is the steady amplitude of the second-order frequency-doubled component, and $\boldsymbol{v}_2^0(\boldsymbol{r})$ is the magnitude of the second-order steady velocity component referred to as the acoustic streaming flow. The orders of magnitude of the three velocity components in the periodic state are given by

$$v_1^\omega \sim Q v_{bc}, \quad v_2^{2\omega} \sim \frac{Q^3 v_{bc}^2}{c_s}, \quad v_2^0 \sim \frac{Q^2 v_{bc}^2}{c_s}. \qquad (27)$$

The order of v_1 is derived in the one-dimensional acoustic cavity example presented in Ref. [32], the order of v_2^0 is given by the well-known Rayleigh theory, while the order of $v_2^{2\omega}$ is derived in the Appendix. The magnitude of $v_2^{2\omega}$ is a factor of Q larger than what is expected from dimensional analysis of the second-order equation (8c). Consequently, the criterion $|v_2| \ll |v_1|$ for the perturbation expansion becomes

$$Q^2 v_{\text{bc}} \ll c_s, \tag{28}$$

which is more restrictive than the usual criterion based on the first-order perturbation expansion, $Q v_{\text{bc}} \ll c_s$. Thus, the perturbation expansion becomes invalid for smaller values of v_{bc} than previously expected.

In the transient regime we cannot Fourier decompose the velocity field. Instead, we propose a decomposition using envelope functions inspired by Eq. (26),

$$\mathbf{v}(\mathbf{r},t) = \mathbf{v}_1^{\omega}(\mathbf{r},t) \sin(\omega t) + \mathbf{v}_2^{2\omega}(\mathbf{r},t) \sin(2\omega t) + \mathbf{v}_2^0(\mathbf{r},t). \tag{29}$$

Here, the amplitudes are slowly varying in time compared to the fast oscillation period t_0. We can no longer separate $\mathbf{v}_2^{2\omega}$ and $\mathbf{v}_2^0$ before solving the second-order time-dependent equations (7) and (8). To obtain the time-dependent magnitude of the quasisteady streaming velocity mode $\mathbf{v}_2^0$, we need to choose a good velocity probe, and we thus form the unsteady time average of $\mathbf{v}_2(\mathbf{r},t)$,

$$\langle \mathbf{v}_2(\mathbf{r},t) \rangle = \int_{t-t_0/2}^{t+t_0/2} \mathbf{v}_2(\mathbf{r},t') dt'. \tag{30}$$

The time averaging is done with a fifth-order Romberg integration scheme [33] using data points with a uniform spacing of $t_0/16$ in the time interval of width t_0.

C. Steady and unsteady streaming flow

In this section we compare the unsteady time-averaged second-order velocity field $\langle \mathbf{v}_2(\mathbf{r},t) \rangle$, from the time-domain simulations, with the steady time-averaged second-order velocity field $\langle \mathbf{v}_2^{\text{fd}}(\mathbf{r},\infty) \rangle$, from the frequency-domain simulation. Figures 4(a) and 4(b) each show a snapshot in time of the transient $\mathbf{v}_1$ and $\mathbf{v}_2$, respectively. For $\mathbf{v}_2(\mathbf{r},t)$, the oscillatory component $\mathbf{v}_2^{2\omega}(\mathbf{r},t) \sin(2\omega t)$ dominates, as it is two orders of magnitude larger than the quasisteady component $\mathbf{v}_2^0(\mathbf{r},t)$. However, at late times, here $t = 3000\,t_0$, the amplitude $\mathbf{v}_2^{2\omega}(\mathbf{r},t)$ has converged, and in $\langle \mathbf{v}_2(\mathbf{r},t) \rangle$ the oscillatory component average to zero and only the quasisteady component remains.

The unsteady time average $\langle \mathbf{v}_2(\mathbf{r},t) \rangle$ evaluated at $t = 3000\,t_0$ is shown in Fig. 4(c), exhibiting a single flow roll, in agreement with the classical Rayleigh streaming flow. In Fig. 4(d) is shown the steady $\langle \mathbf{v}_2^{\text{fd}}(\infty) \rangle$ from the frequency-domain simulation. Figures 4(c) and 4(d) use the same color scaling for the velocity magnitude, to evaluate the convergence of the unsteady streaming flow $\langle \mathbf{v}_2(3000\,t_0) \rangle$ towards the steady streaming flow $\langle \mathbf{v}_2^{\text{fd}}(\infty) \rangle$, and the two solutions agree well both qualitatively and quantitatively. The convergence parameter C, Eq. (19), of $\langle \mathbf{v}_2(3000\,t_0) \rangle$ with respect to $\langle \mathbf{v}_2^{\text{fd}}(\infty) \rangle$ is $C = 0.01$, and if we multiply $\langle \mathbf{v}_2 \rangle$ by a free factor, taking into account that $\langle \mathbf{v}_2 \rangle$ has not fully converged at $t = 3000\,t_0$, the convergence parameter can be reduced to $C = 0.008$. The remaining small
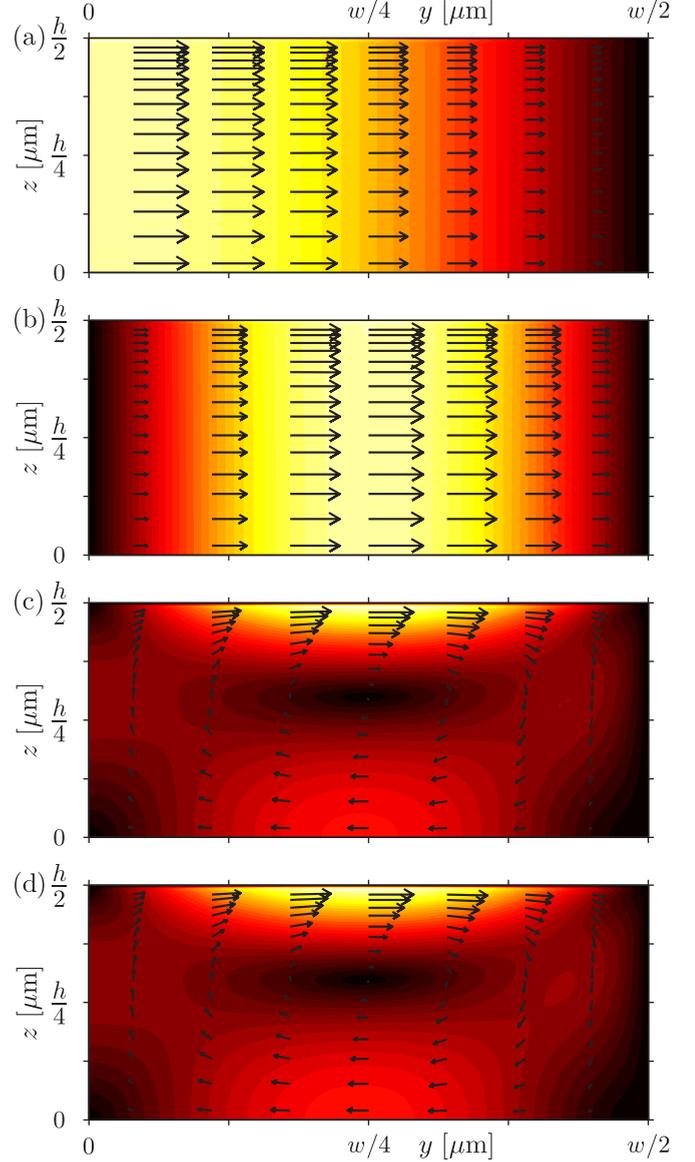

FIG. 4. (Color online) (a) Snapshot of the oscillatory first-order velocity field $\mathbf{v}_1$ (vectors) and its magnitude [color plot ranging from 0 m/s (black) to 0.7 m/s (white)] at $t = 3000\,t_0$. (b) Snapshot of the oscillatory second-order velocity field $\mathbf{v}_2$ (vectors) and its magnitude [color plot ranging from 0 m/s (black) to 0.02 m/s (white)] at $t = 3000\,t_0$. (c) Snapshot of the unsteady time-averaged second-order velocity field $\langle \mathbf{v}_2 \rangle$ (vectors), Eq. (30), and its magnitude [color plot ranging from 0 mm/s (black) to 0.1 mm/s (white)] at $t = 3000\,t_0$. (d) Steady time-averaged second-order velocity field $\langle \mathbf{v}_2^{\text{fd}}(\infty) \rangle$ (vectors), Eqs. (11) and (12), and its magnitude [color scaling as in (c)]. In both the time-domain and the frequency-domain simulations the parameters of the oscillating velocity boundary condition were $\omega = 2\pi f_{\text{res}}$ and $v_{\text{bc}} = \omega d$, with wall displacement $d = 1$ nm.

difference between the unsteady $\langle \mathbf{v}_2(3000\,t_0) \rangle$ and the steady $\langle \mathbf{v}_2^{\text{fd}}(\infty) \rangle$ is attributed to the finite temporal resolution of the time marching scheme. We can thus conclude that the time-domain streaming simulation converges well towards the frequency-domain simulation, and this constitutes the primary validation of the unsteady nonperiodic simulations.
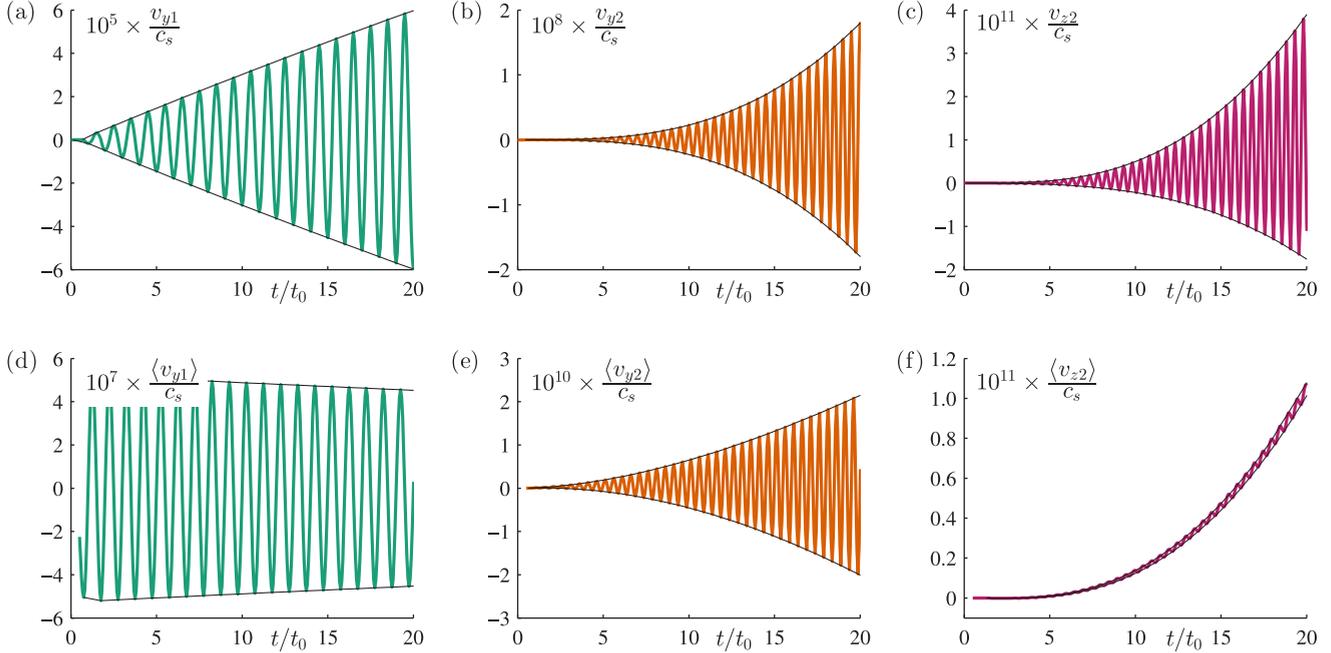
FIG. 5. (Color online) Velocity probes for the initial time interval $0 < t < 20\,t_0$. (a)–(c) Probes for the first- and second-order velocity (a) $v_{y1}(0,0)$, (b) $v_{y2}(w/4,0)$, and (c) $v_{z2}(0,h/4)$. (d)–(f) Running time-average Eq. (30) on an interval one oscillation period wide of the velocity probes in (a)–(c). The thick lines show the oscillating velocity probes while the thin lines emphasize the envelopes of the oscillations.

D. Buildup of the velocity field

To visualize the buildup of the acoustic fields over short and long time scales, we have chosen the three point probes shown in Fig. 1(b). The oscillating first-order velocity field is probed in the center of the channel (0,0), far from the walls in order to measure the bulk amplitude of the acoustic field. The horizontal component of the second-order velocity v_{y2} is probed on the horizontal symmetry axis at $(\frac{1}{4}w,0)$, where the oscillatory component $\boldsymbol{v}_2^{2\omega}$ has its maximum amplitude. The vertical component of the second-order velocity v_{z2} is probed on the vertical symmetry axis at $(0,\frac{1}{4}h)$ where the oscillatory component $\boldsymbol{v}_2^{2\omega}$ is small and of the same order as the quasisteady component $\boldsymbol{v}_2^0$, making the unsteady time-averaged second-order velocity at this point a good probe for the quasisteady streaming velocity.

In Fig. 5 is shown the buildup of the velocity probes [panels (a)–(c)] and their time averages [panels (d)–(f)] for the first 20 oscillations. The thick lines are the oscillating velocities, while the thin lines are the envelopes of the oscillations. Already within the first 20 oscillation periods we see in Fig. 5(f) the buildup of a quasisteady velocity component. The unsteady time-averaged horizontal velocity $\langle v_{y2}\rangle$, Fig. 5(e), is still primarily oscillatory, showing that for this probe the oscillatory component $\boldsymbol{v}_2^{2\omega}$ is much larger than the quasisteady component $\boldsymbol{v}_2^0$.

The temporal evolution of the velocity probes on the longer time scale up to $t = 1500\,t_0$ is shown in Fig. 6. In Figs. 6(a) and 6(b) the amplitudes of the oscillatory first- and second-order velocity components are seen to stabilize around $t = 700\,t_0 \sim 10\,\tau_E$. The steady amplitudes of the velocity probes in Fig. 6 agree with the theoretical predictions of Eq. (27), yielding orders of mag-

nitude $v_1^\omega/c_s \sim 3 \times 10^{-4}$ [Fig. 6(a)], $v_2^{2\omega}/c_s \sim 5 \times 10^{-5}$ [Fig. 6(b)], and $v_2^0/c_s \sim 1 \times 10^{-7}$ [Figs. 6(e) and 6(f)]. The time average of v_{y1} tends to zero for long times as it is purely oscillatory, whereas the time average of v_{y2} tends to the magnitude of the quasisteady component $\boldsymbol{v}_2^0$, because the large but now steady oscillatory component $\boldsymbol{v}_2^{2\omega}$ averages to zero. The dashed lines in Figs. 6(e) and 6(f) represent the magnitude of the steady time-averaged second-order velocity $\langle \boldsymbol{v}_2^{\mathrm{fd}}(\infty)\rangle$ from the frequency-domain simulation.

V. ACOUSTIC STREAMING GENERATED BY PULSED ACTUATION

In the following we study the effects of switching the oscillatory boundary actuation on and off on a time scale much longer than the oscillation period t_0 in either single- or multipulse mode. The aim is to investigate whether such an approach can suppress the influence of the streaming flow on suspended particles relative to that of the radiation force.

A. Single-pulse scaling analysis

A striking feature of Fig. 6 is the separation of time scales between the roughly exponential buildup of the acoustic resonance in Fig. 6(a) and of the streaming flow in Fig. 6(f). It appears that the resonance, and hence the acoustic radiation force on a suspended particle, is fully established almost ten times faster than the streaming flow and the resulting drag force on a suspended particle. To investigate this further, we look at the scaling provided by the three time scales relevant for the problem of transient acoustic streaming, all listed in Table II: the oscillation time t_0 of the acoustic wave, the resonance
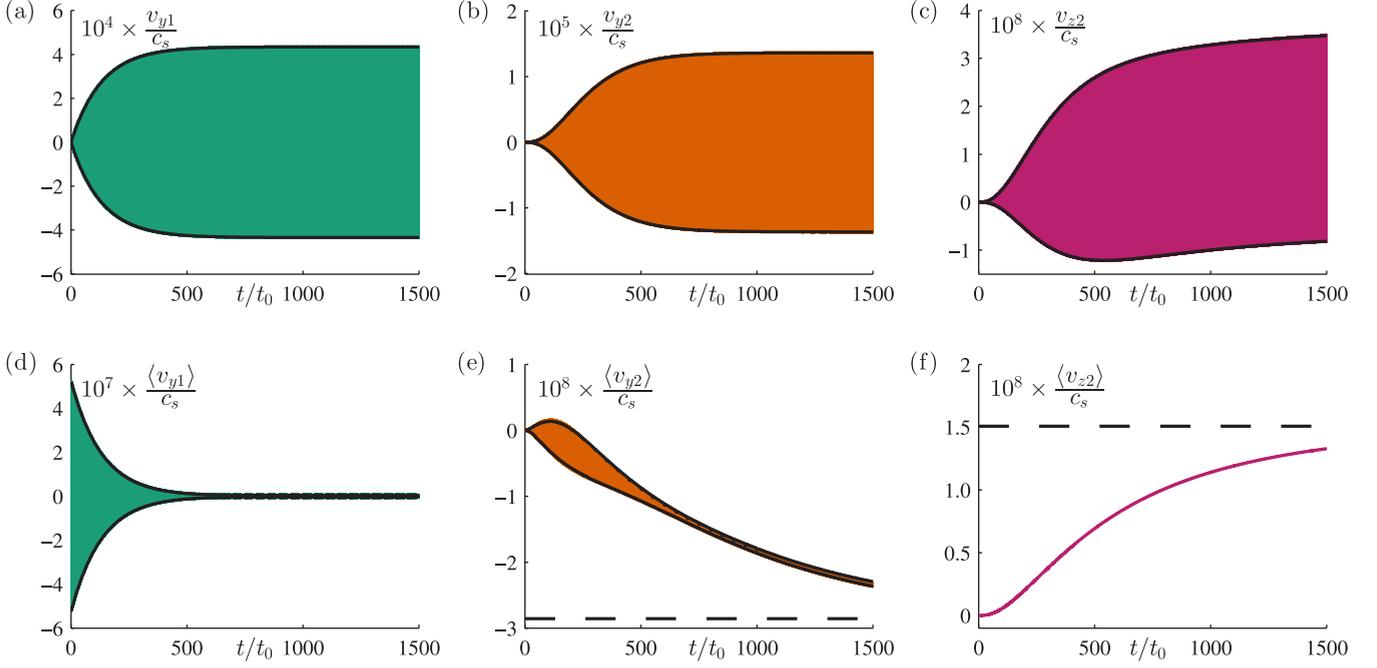
FIG. 6. (Color online) The velocity probes from Fig. 5, but now extended to the long time interval $0 < t < 1500\,t_0$, showing the convergence towards a periodic state. The dashed lines in (e) and (f) indicate the magnitude of the steady time-averaged second-order velocity from the frequency-domain simulation Eqs. (11) and (12).

relaxation time τ_E of the acoustic cavity, and the momentum diffusion time τ_ν governing the quasisteady streaming flow.

The momentum diffusion time is $\tau_\nu = \frac{1}{2\nu}(\frac{1}{8}h)^2$, where $\nu = \frac{\eta}{\rho_0}$ is the kinematic viscosity, and $\frac{1}{8}h$ is approximately half the distance between the top boundary and the center of the streaming flow roll. Inserting the relevant numbers, see Table II, we indeed find that $\tau_E \approx 66\,t_0$ is much faster than $\tau_\nu \approx 558\,t_0$.

While these numbers are obtained for our specific choice of parameters, we can easily establish the scaling for the ratio τ_ν/τ_E as a function of the system parameters in general. For the momentum diffusion time we have $\tau_\nu \propto h^2/\nu$, while the resonance relaxation time at the half-wavelength resonance is $\tau_E \propto Q t_0 \propto \frac{h}{\delta}\frac{1}{\omega} \propto \frac{h}{\sqrt{\nu\omega}} \propto h\sqrt{\frac{w}{\nu}}$. Thus $\tau_\nu/\tau_E \propto \frac{h}{\sqrt{\nu w}}$, and the separation of time scales can be increased in this case by increasing the channel height h, decreasing the channel width w, and decreasing the kinematic viscosity ν.

However, this separation in time scales does not guarantee a suppression of streaming relative to the radiation force. One problem is that the streaming is shear-stress driven in the

TABLE II. Characteristic time scales. The values are obtained by using the kinematic viscosity $\nu = \eta/\rho_0 = 8.93 \times 10^{-7}$ m²/s (Table I), the Q factor $Q = 416$ (Fig. 3), and the channel height $h = 160\,\mu$m (Fig. 1).

Time scale	Expression	Value
Oscillation time	t_0	5.1×10^{-7} s $\approx 1\,t_0$
Resonance relaxation time	$\tau_E = \frac{Q}{2\pi}t_0$	3.4×10^{-5} s $\approx 66\,t_0$
Momentum diffusion time	$\tau_\nu = \frac{1}{2\nu}(\frac{h}{8})^2$	2.8×10^{-4} s $\approx 558\,t_0$

boundary layer, and these stresses build up much faster given the small thickness of the boundary layer. This we investigate further in the following subsection. Another problem is that the large momentum diffusion time τ_ν implies a very slow decay of the streaming flow, once it is established. The latter effect, we study using the following analytical model. Consider a quantity f (streaming velocity or acoustic energy), with a relaxation time τ and driven by a pulsed source term P of pulse width t_{pw}. The rate of change of f is equivalent to Eq. (14b),

$$\partial_t f = P - \frac{1}{\tau}f, \tag{31a}$$

$$P = \begin{cases} \frac{1}{\tau}f_0, & \text{for } 0 < t < t_{pw}, \\ 0, & \text{otherwise}, \end{cases} \tag{31b}$$

where $\frac{1}{\tau}f_0$ is a constant input power. This simplified analytical model captures the roughly exponential buildup and decay characteristics of our full numerical model, and allows for analytical studies of the time integral of $f(t)$. For a final time $t > t_{pw}$ we find

$$\int_0^t f(t')\,dt' = f_0 t_{pw} - f_0\tau\big[e^{-\frac{1}{\tau}(t-t_{pw})} - e^{-\frac{1}{\tau}t}\big]. \tag{32}$$

From this we see that when $t \gg \tau + t_{pw}$ the time-integral of $f(t)$ is approximately $f_0 t_{pw}$ and not dependent on the relaxation time τ. Consequently, if both the acoustic energy and the acoustic streaming can be described by exponential behavior with the respective relaxation times τ_E and τ_ν, the ratio of their time-integrated effects is the same whether the system is driven by a constant actuation towards their steady time-periodic state or by a pulsed actuation with pulse width t_{pw}. This simplified analytical model indicates that there is little
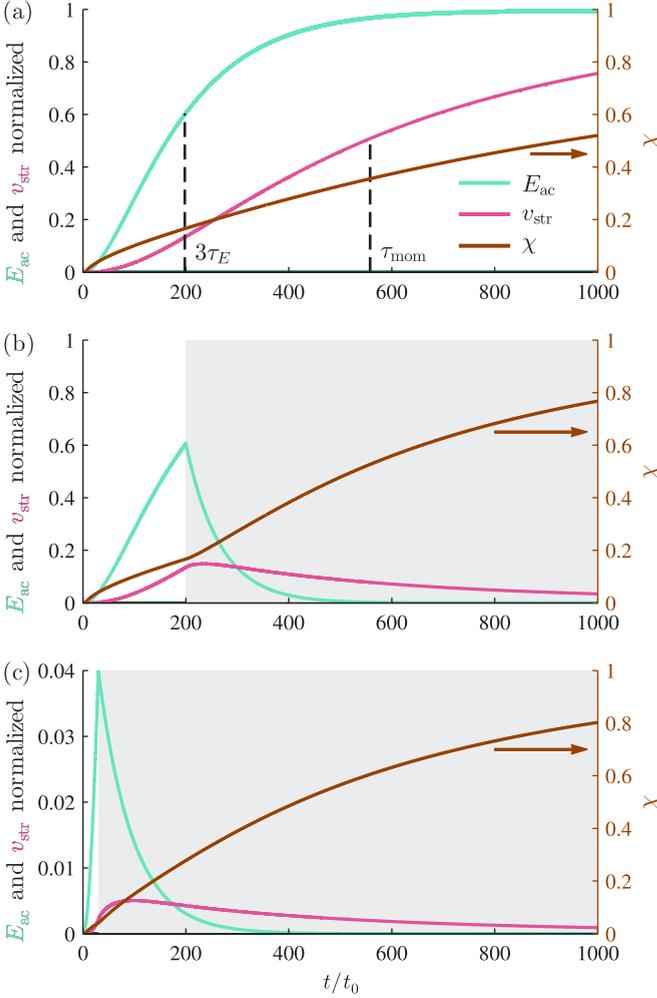
FIG. 7. (Color online) Acoustic energy $\langle E_{ac}(t)\rangle/\langle E_{ac}^{fd}(\infty)\rangle$ Eq. (13) (light green), streaming velocity $\langle v_{str}(t)\rangle/\langle v_{str}^{fd}(\infty)\rangle$ Eq. (33) (medium purple), and streaming ratio $\chi(t)$ Eq. (34) (dark brown, right ordinate axis). The gray background indicates the time intervals where the actuation is turned off. (a) Constant actuation for $0 < t < 3000\,t_0$. (b) Actuation on for $0 < t < 200\,t_0$ followed by no actuation for $200\,t_0 < t < 1000\,t_0$. (c) Actuation on for $0 < t < 30\,t_0$ followed by no actuation for $30\,t_0 < t < 1000\,t_0$.

hope of decreasing acoustic streaming relative to the acoustic radiation force by applying pulsed actuation, in spite of the order of magnitude difference between the relaxation times for the acoustic energy and the streaming.

B. Single-pulse numerical simulation

We investigate the features of pulsed actuation in more detail in the following by numerical simulation. In Fig. 7 is shown the temporal evolution of the total acoustic energy $\langle E_{ac}\rangle$ and the magnitude of the acoustic streaming flow $\langle v_{str}\rangle$ for the three cases: (i) the buildup towards the periodic state, (ii) a single long actuation pulse, and (iii) a single short actuation pulse. The magnitude of the acoustic streaming is measured by the unsteady time-averaged velocity probe

$$\langle v_{str}\rangle = \langle v_{z2}(0, \tfrac{1}{4}h)\rangle, \tag{33}$$

and the unsteady energy and streaming probes obtained from the time-domain simulation are normalized by their corresponding steady time-averaged values from the frequency-domain simulation.

We introduce the streaming ratio χ to measure the influence of streaming-induced drag on suspended particles relative to the influence of the acoustic radiation force for the unsteady time-domain solution, in comparison to the periodic frequency-domain solution. To calculate the relative displacement Δs of particles due to each of the two forces, respectively, we compare their time integrals. Since the radiation force scales with the acoustic energy density, we define the streaming ratio $\chi(t)$ as

$$\chi(t) = \frac{\int_0^t \frac{\langle v_{str}(t')\rangle}{\langle v_{str}^{fd}(\infty)\rangle}\,dt'}{\int_0^t \frac{\langle E_{ac}(t')\rangle}{\langle E_{ac}^{fd}(\infty)\rangle}\,dt'} \sim \frac{\frac{\Delta s_{str}}{\Delta s_{str}^{fd}}}{\frac{\Delta s_{rad}}{\Delta s_{rad}^{fd}}}, \tag{34}$$

where Δs_{str} and Δs_{rad} are the total particle displacements in the time from 0 to t due to the streaming-induced drag force and the acoustic radiation force, respectively. In the periodic state $\chi = 1$, and to obtain radiation-force-dominated motion of smaller particles, we need to achieve a smaller value of χ. Obtaining a value of $\chi = 0.8$ at time t_{end} implies that the ratio of the relative displacement due to the streaming-induced drag force and the radiation force for the time interval $0 < t < t_{end}$ is 20% lower than in the periodic state, corresponding to a 20% reduction of the critical particle size for acoustophoretic focusing, defined in Ref. [2], assuming the particles can be focused during the time interval $0 < t < t_{end}$.

Figure 7(a) shows $\langle E_{ac}\rangle$, $\langle v_{str}\rangle$, and χ during the buildup towards the periodic state. χ approaches unity slower than $\langle v_{str}\rangle$ because χ is an integration of the streaming and radiation contributions, whereas v_{str} probes the instantaneous magnitude of the streaming flow. Figure 7(b) and 7(c) show $\langle E_{ac}\rangle$, $\langle v_{str}\rangle$, and χ when the actuation is turned off at $t = 200\,t_0$ and $t = 30\,t_0$, respectively. When the actuation is turned off, $\langle E_{ac}\rangle$ decays faster than $\langle v_{str}\rangle$ and thus χ begins to increase more rapidly, reaching $\chi = 0.8$ around $t = 1000\,t_0$ in both cases. From the results shown in Fig. 7 it does not seem advantageous to turn off the actuation, as this only causes χ to increase faster than for constant actuation. Figure 7(c) further shows that when the actuation is turned off, $\langle E_{ac}\rangle$ immediately begins to decay, whereas $\langle v_{str}\rangle$ continues to increase for some time, due to the present acoustic energy in the system that still provides a driving force for the streaming flow.

C. Multipulse numerical simulation

From the single-pulse results shown in Fig. 7 there is no indication of any optimum for the pulse duration or repetition period, and in general it provides little hope that pulsed actuation should lead to lower values of χ. Figure 8 shows $\langle E_{ac}\rangle$, $\langle v_{str}\rangle$, and χ for three pulsed schemes with pulse duration $500\,t_0$, $200\,t_0$, and $30\,t_0$ and pause duration $500\,t_0$, $200\,t_0$, and $210\,t_0$, respectively. For all three pulsed schemes, χ increases faster than for the constant actuation Fig. 7(a), thus not indicating any increased suppression of the streaming.
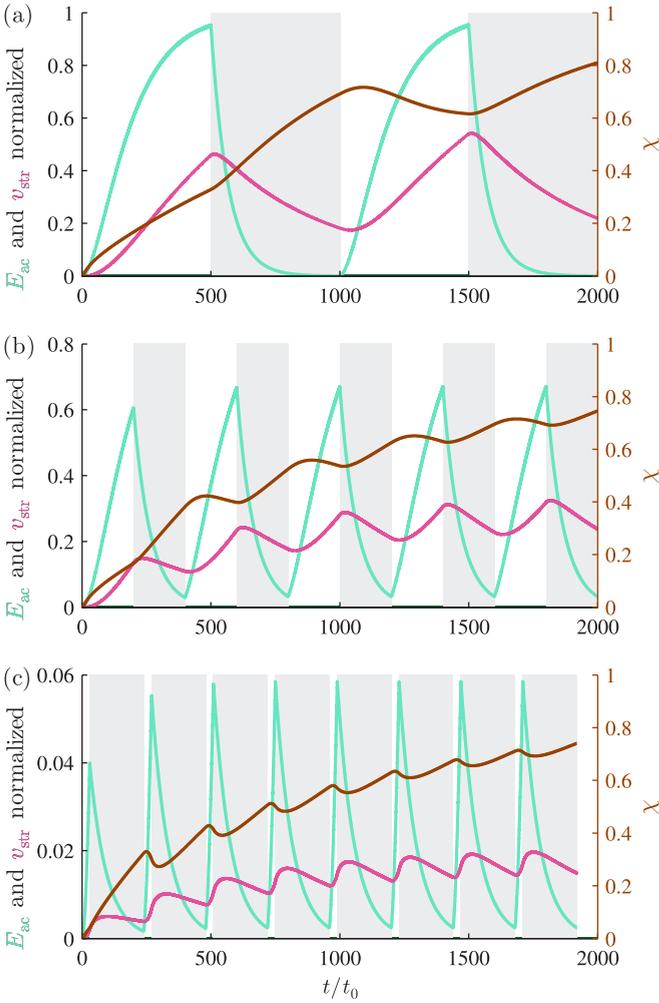
FIG. 8. (Color online) The same probes as in Fig. 7 but for the following pulsed actuation schemes: (a) actuation is on for $500\,t_0$ followed by no actuation for $500\,t_0$ repeatedly, (b) actuation is on for $200\,t_0$ followed by no actuation for $200\,t_0$ repeatedly, and (c) actuation is on for $30\,t_0$ followed by no actuation for $210\,t_0$ repeatedly.

VI. DISCUSSION

Solving numerically the time-dependent problem of the acoustic cavity and the buildup of acoustic streaming presents new challenges which are not present in the purely periodic problem. First, the numerical convergence analysis now involves both the spatial and temporal resolutions. This we addressed in a sequential process by first analyzing the spatial mesh with the periodic frequency-domain solution, and thereafter doing a thorough convergence analysis with respect to the temporal resolution. Second, the convergence of the transient solution towards the periodic state was poor for actuation frequencies away from the resonance frequency of the system. This makes off-resonance simulation computationally costly, as it requires a better temporal resolution, and it complicates comparison of simulations at resonance with simulations off resonance. Third, small numerical errors accumulate during the hundred thousand time steps taken during a simulation from a quiescent state to a purely periodic state. These errors need to be suppressed by the

numerical time-domain solver, which in the generalized-alpha solver is done through the alpha parameter. Simulation with higher temporal resolution required lower values of the alpha parameter to have more suppression of accumulated numerical errors.

The model system used in this study is a simplification of an actual device. The vibration of only the side walls, and not the top and bottom walls, stands in contrast to the physical system, in which the whole device is vibrating in a nontrivial way, difficult to predict, and only the overall amplitude and the frequency of the actuation is controlled experimentally. Furthermore, our model only treats the two-dimensional cross section of a long straight channel, whereas experimental studies have shown that there are dynamics along the length of the channel [21]. Nevertheless, successful comparisons, both qualitatively and quantitatively, have been reported between the prediction of this simplified numerical model and experimental measurements of Rayleigh streaming in the cross-sectional plane of a microchannel [10], which makes it reasonable to assume that the time-dependent simulations also provide reliable predictions.

It is also important to stress that our model only describes the fluid and not the motion of the suspended particles. Integrating the forces acting on the particles becomes vastly more demanding when the streaming flow is unsteady, because the drag forces from the oscillating velocity components $\boldsymbol{v}_1$ and $\boldsymbol{v}_2^{2\omega}$ do not average out, as they do in the case of a purely time-periodic state. To include this contribution in the particle tracking scheme, the forces on the particles need to be integrated with a time step of a fraction of the oscillation period, which makes the solution of particle trajectories over several seconds a very demanding task using brute-force integration of the equations of motion.

Our analysis of the pulsed actuation schemes showed that the slow decay of the streaming flow makes pulsation inefficient in reducing the streaming-induced drag force compared to the radiation force. Such a reduction may, however, be obtained by a rapid switching between different resonances each resulting in similar radiation forces but different spatial streaming patterns which on average cancel each other out, thus fighting streaming with streaming. An idea along these lines was presented by Ohlin *et al.* [34], who used frequency sweeping to diminish the streaming flows in liquid-filled wells in a multiwell plate for cell analysis. However, the prediction of particle trajectories under such multiresonance conditions requires an extensive study as described above.

To our knowledge, experimental studies of pulsed actuation to decrease streaming flow have so far only been reported in the literature by Hoyos *et al.* [18]. Unfortunately, their study is not directly comparable to our analysis, as we treat the buildup of Rayleigh streaming perpendicular to the pressure nodal plane, whereas Hoyos *et al.* studied the streaming flow in this plane. Such in-nodal-plane streaming flows have been studied numerically by Lei *et al.* [12,13], though only with steady actuation. The contradicting results of our numerical study and the experimental study of Hoyos *et al.* may thus rely on the differences of the phenomena studied. However, despite the negative result presented above, we nevertheless hope that our analysis may serve as an inspiration for future experimental and numerical studies of acoustic streaming induced by pulsed

actuation. We would certainly be interested in applying our analysis to future, well-characterized experimental studies of such pulse-actuated streaming.

VII. CONCLUSION

In this work, we have presented a model for the transient acoustic fields and the unsteady time-averaged second-order velocity field in the transverse cross-sectional plane of a long straight microchannel. The model is based on the usual perturbation approach for low acoustic field amplitudes, and we have solved both first- and second-order equations in the time domain for the unsteady transient case as well as in the frequency domain for the purely periodic case. This enabled us to characterize the buildup of the oscillating acoustic fields and the unsteady streaming flow.

Our analysis has shown that the buildup of acoustic energy in the channel follows the analytical prediction obtained for a single damped harmonic oscillator with sinusoidal forcing, and that a quasisteady velocity component is established already within the first few oscillations and increases in magnitude as the acoustic energy builds up. We have also found that for a resonance with quality factor Q, the amplitude of the oscillatory second-order velocity component is a factor of Q larger than what is expected from dimensional analysis, which results in a more restrictive criterion for the validity of the perturbation expansion, compared to the usual one based on the first-order perturbation expansion.

Furthermore, contrary to a simple scaling analysis of the time scales involved in the fast buildup of radiation forces and slow buildup of drag-induced streaming forces, we have found that pulsating oscillatory boundary actuation does not reduce the time-integrated streaming-induced drag force relative to the time-integrated radiation force. As a result, pulsating actuation does not prevent streaming flows perpendicular to the pressure nodal plane from destroying the ability to focus small particles by acoustophoresis.

ACKNOWLEDGMENT

APPENDIX: AMPLITUDE OF THE SECOND-ORDER OSCILLATORY VELOCITY FIELD

Extending to second order the one-dimensional example given in Ref. [32], we derive in this Appendix the order of magnitude of the second-order oscillatory component $v_2^{2\omega}$, which was stated in Eq. (27).

Just as $\langle g_2 \rangle$ denotes time-averaging over one oscillation period, Eq. (30), and in the periodic state equals the zero-order temporal Fourier component of the field, $g_2^{2\omega}(\boldsymbol{r})$ denotes the complex amplitude of the oscillatory second-order mode and is given by the second-order Fourier component,

$$g_2^{2\omega}(\boldsymbol{r}) = \frac{1}{T} \int_{t-T/2}^{t+T/2} g_2(\boldsymbol{r},t')e^{-i2\omega t'}\, dt'. \quad \text{(A1)}$$

By using that for any complex number Z we have $\mathrm{Re}[Z] = \frac{1}{2}(Z + Z^*)$, the product $A(\boldsymbol{r},t)B(\boldsymbol{r},t)$ of two oscillating fields $A(\boldsymbol{r},t) = \mathrm{Re}[Ae^{-i\omega t}]$ and $B(\boldsymbol{r},t) = \mathrm{Re}[Be^{-i\omega t}]$ can be decomposed into a steady component and an oscillatory component,

$$\begin{aligned} A(t)B(t) &= \tfrac{1}{2}(Ae^{-i\omega t} + A^* e^{i\omega t})\tfrac{1}{2}(Be^{-i\omega t} + B^* e^{i\omega t}) \\ &= \tfrac{1}{2}\mathrm{Re}[A^* B] + \tfrac{1}{2}\mathrm{Re}[ABe^{-i2\omega t}], \quad \text{(A2)} \end{aligned}$$

from which we introduce the following notation:

$$\langle AB \rangle \equiv \tfrac{1}{2}\mathrm{Re}[A^* B], \quad (AB)^{2\omega} \equiv \tfrac{1}{2}AB, \quad \text{(A3)}$$

where A and B could be any first-order fields.

The governing equations for the oscillatory second-order component $\boldsymbol{v}_2^{2\omega}$ can be derived from Eqs. (7) and (8), and in the one-dimensional problem treated in Ref. [32], where the top and bottom walls are not taken into account, they become

$$-i2\omega\kappa_s p_2^{2\omega} = -\partial_y v_2^{2\omega} - \kappa_s(v_1 \partial_y p_1)^{2\omega}, \quad \text{(A4a)}$$

$$\begin{aligned} -i2\omega\rho_0 v_2^{2\omega} = -\partial_y p_2^{2\omega} + \left(\tfrac{4}{3}\eta + \eta^{\mathrm{b}}\right)\partial_y^2 v_2^{2\omega} \\ - [\rho_1(-i\omega v_1)]^{2\omega} - \rho_0(v_1 \partial_y v_1)^{2\omega}. \quad \text{(A4b)} \end{aligned}$$

Applying the 2ω rule (A3) and mass continuity (5), the two last terms of Eq. (A4b) cancel. Inserting Eq. (A4a) into Eq. (A4b), the governing equation for $v_2^{2\omega}$ becomes

$$4k_0^2 v_2^{2\omega} + (1 - i4\Gamma)\partial_y^2 v_2^{2\omega} + \tfrac{1}{2}\kappa_s \partial_y(v_1 \partial_y p_1) = 0, \quad \text{(A5)}$$

where Γ is the nondimensional bulk damping coefficient given by $\Gamma = \frac{\omega\eta}{2\rho_0 c_s^2}\left(\frac{4}{3} + \frac{\eta^{\mathrm{b}}}{\eta}\right)$, and $k_0 = \frac{\omega}{c_s}$ is the wave number. For the fundamental half-wave resonance, the spatial dependence of the source term $\partial_y(v_1 \partial_y p_1)$ is $\sin(2k_0 y)$, and the guess for the inhomogeneous solution to Eq. (A5) thus becomes

$$v_2^{2\omega,\mathrm{inhom}} = C \sin(2k_0 y). \quad \text{(A6)}$$

Inserting the inhomogeneous solution Eq. (A6) into the governing equation (A5), we note that the first term cancels with the "1" in the parentheses of the second term, and the order of magnitude of the inhomogeneous solution thus becomes

$$\left| v_2^{2\omega} \right| = C \sim \frac{1}{\Gamma}\kappa_s|v_1||p_1| \sim \frac{1}{\Gamma^3}\frac{v_{\mathrm{bc}}^2}{c_s} \sim Q^3 \frac{v_{\mathrm{bc}}^2}{c_s}, \quad \text{(A7)}$$

which is the result stated in Eq. (27).

[1] H. Bruus, J. Dual, J. Hawkes, M. Hill, T. Laurell, J. Nilsson, S. Radel, S. Sadhal, and M. Wiklund, Lab Chip **11**, 3579 (2011).

[2] P. B. Muller, R. Barnkob, M. J. H. Jensen, and H. Bruus, Lab Chip **12**, 4617 (2012).

[3] R. Barnkob, P. Augustsson, T. Laurell, and H. Bruus, Phys. Rev. E **86**, 056307 (2012).

[4] L. Rayleigh, Philos. Trans. R. Soc. London **175**, 1 (1884).

[5] H. Schlichting, Phys. Z. **33**, 327 (1932).

[6] W. L. Nyborg, J. Acoust. Soc. Am. **30**, 329 (1958).

[7] M. Hamilton, Y. Ilinskii, and E. Zabolotskaya, J. Acoust. Soc. Am. **113**, 153 (2003).

[8] M. Hamilton, Y. Ilinskii, and E. Zabolotskaya, J. Acoust. Soc. Am. **114**, 3092 (2003).

[9] A. Y. Rednikov and S. S. Sadhal, J. Fluid Mech. **667**, 426 (2011).

[10] P. B. Muller, M. Rossi, A. G. Marin, R. Barnkob, P. Augustsson, T. Laurell, C. J. Kähler, and H. Bruus, Phys. Rev. E **88**, 023006 (2013).

[11] P. B. Muller and H. Bruus, Phys. Rev. E **90**, 043016 (2014).

[12] J. Lei, P. Glynne-Jones, and M. Hill, Lab Chip **13**, 2133 (2013).

[13] J. Lei, M. Hill, and P. Glynne-Jones, Lab Chip **14**, 532 (2014).

[14] W. L. Nyborg, J. Acoust. Soc. Am. **25**, 68 (1953).

[15] C. Lee and T. Wang, J. Acoust. Soc. Am. **85**, 1081 (1989).

[16] P. Hahn and J. Dual, Phys. Fluids **27**, 062005 (2015).

[17] N. Nama, R. Barnkob, Z. Mao, C. J. Kähler, F. Costanzo, and T. J. Huang, Lab Chip **15**, 2700 (2015).

[18] M. Hoyos and A. Castro, Ultrasonics **53**, 70 (2013).

[19] M. Antfolk, P. B. Muller, P. Augustsson, H. Bruus, and T. Laurell, Lab Chip **14**, 2791 (2014).

[20] J. Wang and J. Dual, J. Phys. A: Math. Theor. **42**, 285502 (2009).

[21] P. Augustsson, R. Barnkob, S. T. Wereley, H. Bruus, and T. Laurell, Lab Chip **11**, 4152 (2011).

[22] A. D. Pierce, *Acoustics* (Acoustical Society of America, Woodbury, 1991).

[23] L. D. Landau and E. M. Lifshitz, *Statistical Physics, Part 1*, 3rd ed., Vol. 5 (Butterworth-Heinemann, Oxford, 1980).

[24] COMSOL Multiphysics 4.4, http://www.comsol.com.

[25] S. C. Brenner and L. R. Scott, *The Mathematical Theory of Finite Element Methods* (Springer, New York, 2008).

[26] K. E. Jansen, C. H. Whiting, and G. M. Hulbert, Comput. Methods Appl. Mech. Eng. **190**, 305 (2000).

[27] COMSOL Multiphysics Reference Manual, Ver. 4.4, 2013.

[28] COMSOL Multiphysics support website http://www.comsol.dk/support/knowledgebase/1062.

[29] MATLAB 2012a, http://www.mathworks.com.

[30] See Supplemental Material at http://link.aps.org/supplemental/10.1103/PhysRevE.92.063018 for COMSOL model files, both in a simple version Muller2015_TimeDepAcoust_simple.mph and a full version Muller2015_TimeDepAcoust_full.mph that allows for sectioning in smaller time intervals using the supplied MATLAB script Muller2015_TimeDepAcoust_full.m.

[31] COMSOL Multiphysics Model Library, Nonlinear Acoustics— Modeling of the 1D Westervelt Equation, 2013.

[32] H. Bruus, Lab Chip **12**, 20 (2012).

[33] W. H. Press, S. A. Teukolsky, W. T. Vetterling, and B. P. Flannery, *Numerical Recipes in C: The Art of Scientific Computing*, 2nd ed. (Cambridge University Press, Cambridge, 2002).

[34] M. Ohlin, A. Christakou, T. Frisk, B. Önfelt, and M. Wiklund, in *Proc. 15th MicroTAS, 2–6 October 2011, Seattle (WA), USA*, edited by J. Landers, A. Herr, D. Juncker, N. Pamme, and J. Bienvenue (The Printing House, Inc., Stoughton, WI, 2011), pp. 1612–1614.